Real-Time Monitoring of Arsenic Trioxide Release and Delivery by Activatable T_1 Imaging

Zhenghuan Zhao,[†] Xiaomin Wang,[‡] Zongjun Zhang,[†] Hui Zhang,[†] Hanyu Liu,[†] Xianglong Zhu,[†] Hui Li,[‡] Xiaoqin Chi,[‡] Zhenyu Yin,[‡] and Jinhao Gao*[,†]

[†]State Key Laboratory of Physical Chemistry of Solid Surfaces, The Key Laboratory for Chemical Biology of Fujian Province, and Department of Chemical Biology, College of Chemistry and Chemical Engineering, Xiamen University, Xiamen 361005, China, and [‡]Fujian Provincial Key Laboratory of Chronic Liver Disease and Hepatocellular Carcinoma, Zhongshan Hospital, Xiamen University, Xiamen 361004, P. R. China

ABSTRACT Delivery of arsenic trioxide (ATO), a clinical anticancer drug, has drawn much attention to improve its pharmacokinetics and bioavailability for efficient cancer therapy. Real-time and *in situ* monitoring of ATO behaviors *in vivo* is highly desirable for efficient tumor treatment. Herein, we report an ATO-based multifunctional drug delivery system that efficiently delivers ATO to treat tumors and allows real-time monitoring of ATO release by activatable T_1 imaging. We loaded water-insoluble manganese arsenite complexes, the ATO prodrug, into hollow silica nanoparticles to form a pH-sensitive multifunctional drug delivery system. Acidic stimuli triggered the simultaneous release of manganese ions and ATO, which dramatically increased the T_1 signal (bright signal) and enabled real-time visualization and monitoring of ATO release and delivery. Moreover, this smart multifunctional drug delivery system significantly improved ATO efficacy and strongly inhibited the growth of solid tumors without adverse side effects. This strategy has great potential for real-time monitoring of theranostic drug delivery in cancer diagnosis and therapy.

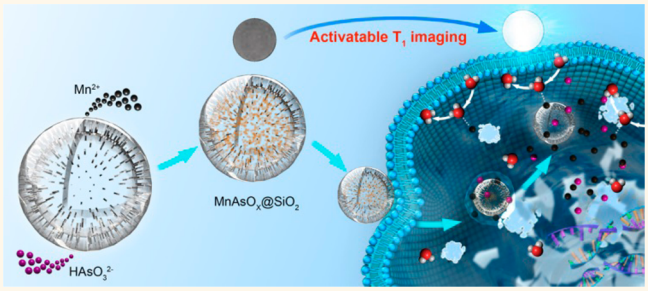

KEYWORDS: arsenic trioxide · activatable T_1 imaging · monitoring · cancer diagnosis · cancer therapy

Chemotherapy is the dominant treatment modality for cancer, yet it is limited by poor biodistribution and severe side effects in patients.[1−5] To address these limitations, multifunctional drug delivery systems (MDDSs), in which medical diagnostics, drug delivery, and therapy are integrated into a single nanosystem, have emerged as a promising approach to improve the efficacy of chemotherapy.[6−9] Arsenic trioxide (ATO, As_2O_3) is a U.S. Food and Drug Administration (FDA) approved front-line agent for the treatment of acute promyelocytic leukemia (APL).[10−12] ATO exerts high cytotoxicity to various types of cancer cells, including breast, liver, and prostate, by induction of apoptosis. Moreover, ATO can promote the differentiation, inhibit the migration, and reduce the invasion of surviving cancer cells,[11] indicating that ATO may have higher therapeutic effect with lower risk of recurrence and metastasis than the traditional anticancer drugs (*e.g.*, DOX and PTX). This unique ability allows ATO to be a potential candidate to treat hepatocellular carcinoma, which is one of the most threatening and common cancers with high recurrence for humans in the world, especially China. Drug delivery systems allow ATO to achieve a high therapeutic effect with a low risk of recurrence and side effects. For example, liposome and inorganic nanomaterial-based vehicles have been employed to deliver ATO for efficient cancer treatment.[13,14] However, these single-function drug delivery systems are unable to track drug biodistribution *in situ*, which is critical for evaluating the delivery and therapeutic efficiency of the drug.[15,16] Therefore, the rationally designed MDDSs for both real-time monitoring of ATO drug and efficient tumor treatment are necessary but remain challenging.

Currently, there are two major strategies for the fabrication of multifunctional drug delivery systems. The most common. strategy

* Address correspondence to jhgao@xmu.edu.cn.

Received for review November 21, 2014 and accepted February 17, 2015.

Published online February 17, 2015
10.1021/nn506640h

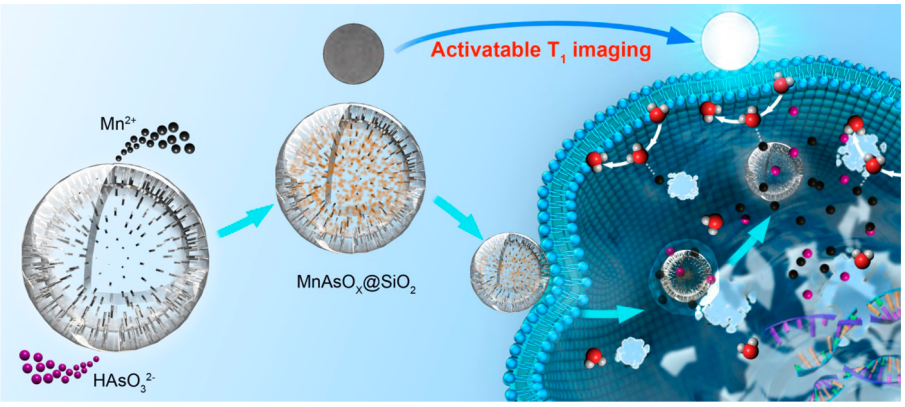

Scheme 1. Schematic Cartoon of Compatible Loading of ATO in Hollow Silica Nanoparticles and Its Drug Release with Activatable T_1 Imaging Process Inside Cells

is to use fluorescent drugs as model cargos. This strategy allows real-time monitoring of drug behavior by fluorescence resonance energy transfer (FRET).[17−20] However, this system exhibited low penetration depth in living tissues due to its UV or visible light excitation source, which severely limits its application in clinic. Another strategy is to link the chemotherapeutic drug to various types of functional nanomaterials, such as iron oxide nanoparticles,[21−25] gold nanostructures,[26,27] and inorganic fluorescent nanomaterials.[28−30] Unfortunately, because this strategy monitors the behavior of the vehicles rather than the drugs, it is unable to monitor drug delivery and release. Recently, activatable longitudinal relaxation time (T_1) magnetic resonance imaging (MRI) contrast agents have been designed to respond to specific changes in the surrounding physiological microenvironment, potentially allowing MRI technology to detect biological processes associated with enzymatic activity and disease.[31−35] Activatable T_1 imaging produces noninvasive and tissue-depth-independent images with high spatial and temporal resolution. Additionally, it induces a fast T_1 relaxation and results in a significant amplification of T_1 signal under specific stimuli. Due to these unique features, activatable T_1 imaging may be a favorable tool for real-time monitoring and quantitative assessment of drug release *in vivo*.

Typical activatable T_1 imaging is highly dependent on certain properties of the T_1 contrast agents, such as the number of coordinated water molecules (q), proton residence lifetime (τ_m), and molecular tumbling time (τ_R).[36] Therefore, a contrast agent must have suitable properties to establish a successful activatable T_1 imaging system. Gd-based chelates are the major T_1 contrast agents used in the clinic. Unfortunately, their clinical use has been restricted by the FDA due to a possible link between Gd-containing contrast agents and nephrogenic systemic fibrosis (NSF).[37,38] To increase the safety of MRI contrast agents, much emphasis is now being placed on alternative approaches based on nonlanthanide metals, in particular manganese ions (Mn^{2+}). Mn^{2+} is a typical T_1 contrast agent with high spin number, long electronic relaxation time, and labile water exchange.[39,40] Because Mn^{2+} is critical in cell biology (*e.g.*, Mn^{2+} often acts as a cofactor for enzymes and receptors), various materials based on Mn^{2+}, such as $MnCl_2$,[41,42] manganese chelates,[43] and MnO nanoparticles,[44,45] have been used to diagnose cancer with good biocompatibility. More importantly, in the presence of As(III) ions, Mn^{2+} can form complexes that are insoluble in pH-neutral environments but can collapse in acidic environments.[46] By increasing the efficiency of direct chemical exchange between metal centers and surrounding protons, this pH-dependent process can switch on the T_1 signal, thus establishing an activatable T_1 imaging system.[47,48] Because of these characteristics, Mn^{2+} ions are one of the best activatable T_1 contrast agents for monitoring ATO drug release and delivery in real time.

Herein, we report an ATO-based MDDS that efficiently treats tumors and monitors ATO controlled release by activatable T_1 imaging *in vitro* and *in vivo*. We use hollow silica nanoparticles to load water-insoluble manganese-arsenite complexes to create a pH-sensitive MDDS. This smart MDDS can simultaneously diagnose tumors accurately, monitor ATO drug delivery and release in real time, and provide efficient anticancer therapy *in vivo*. These properties allow this novel drug delivery system to achieve concurrent monitoring and treatment of solid tumors, thus providing increased insight into drug pharmacokinetics, local response, and overall efficacy.

RESULTS AND DISCUSSION

Synthesis and Characterization. The $MnAsO_x@SiO_2$ nanomaterials were prepared *via* ion gradient mediated loading. As illustrated in Scheme 1, we mixed the as-prepared hollow silica nanoparticles (HSNs) with aqueous manganese chloride and subsequently with ATO. During the loading process, the Mn^{2+} and $HAsO_3^{2-}$ ions (denoted as Mn and As, respectively) can

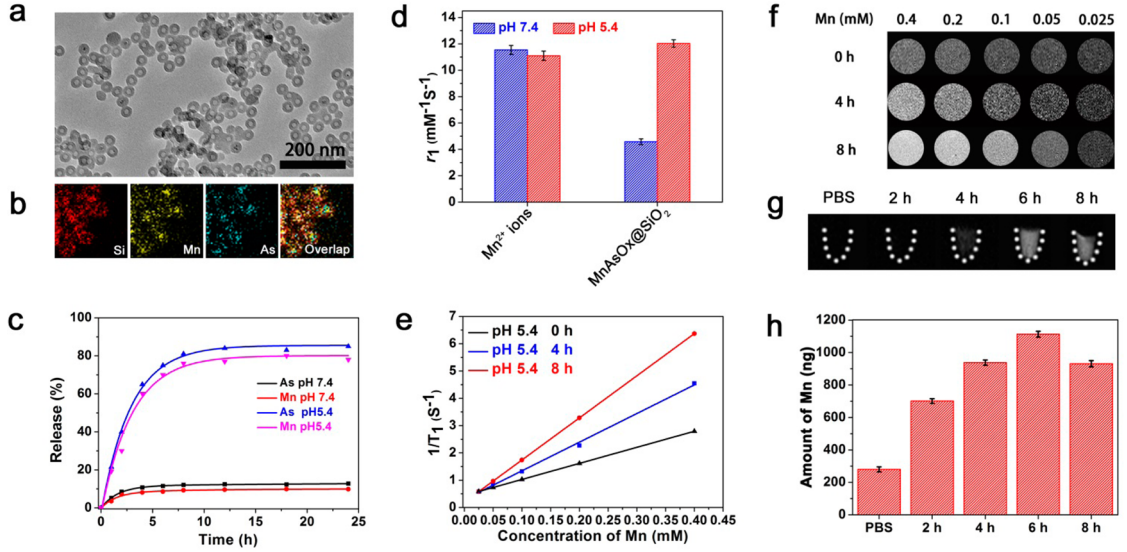

Figure 1. Characterization of $MnAsO_x@SiO_2$ drug delivery system. (a) TEM image of $MnAsO_x@SiO_2$ consisting of the core/shell structure with high yield. (b) EDX mapping images of the $MnAsO_x@SiO_2$ nanoparticles, indicating that the location of Mn and As elements are in the core of HSNs. (c) Release profiles of Mn and As ions from HSNs at different pH values of 7.4 and 5.4. (d) r_1 values of Mn ions and $MnAsO_x@SiO_2$ in the buffer with the pH values of 7.4 and 5.4. (e) Analysis of relaxation rate R_1 ($1/T_1$) vs Mn concentration for $MnAsO_x@SiO_2$ incubated in the pH 5.4 buffer for 0, 4, and 8 h. (f) T_1-weighted MR images of $MnAsO_x@SiO_2$ incubated in the buffer (pH 5.4) for 0, 4, and 8 h. (g) T_1-weighted MR images of SMMC-7721 cells incubated with $MnAsO_x@SiO_2$ for different time durations. (h) Total amount of Mn ions in SMMC-7721 cancer cells incubated with $MnAsO_x@SiO_2$ for different times. The concentration of Mn was tested by ICP-MS (n = 3/group).

diffuse across the shell of the HSNs and form insoluble manganese arsenite complexes, $[Mn(HAsO_3)]_n$ (denoted as $MnAsO_x$), in the hollow interiors of the HSNs. After centrifugation and purification, we obtained the $[Mn(HAsO_3)]_n@SiO_2$ nanomaterials (denoted as $MnAsO_x@SiO_2$) in aqueous solution. Transmission electron microscopy (TEM) images showed that the as-prepared product was highly uniform, with a diameter of 40 ± 2 nm (Figure 1a). Dynamic light scattering (DLS) analysis indicated that the $MnAsO_x@SiO_2$ was monodisperse in water with a hydrodynamic diameter (HD) of 55 ± 3 nm (Supporting Information, Figure S1). These results suggested that the $MnAsO_x@SiO_2$ was well-dispersed in water without any clustering or aggregation. The small increase in HD could be attributed to the hydration layer on the surface of the nanomaterials.[49] To confirm the successful fabrication of $MnAsO_x@SiO_2$, we conducted TEM-associated energy dispersive X-ray spectroscopy (EDS) analysis and energy-dispersive X-ray element mapping (EDX mapping). EDS analysis showed a high intensity signal at typical peaks of Mn and As, indicating successful accumulation of Mn and As in the MDDS (Supporting Information, Figure S2). In agreement with the EDS results, EDX mapping indicated that there were ample Mn and As atoms in the core of the HSNs (Figure 1b). These two analyses indicated that we successfully synthesized a $MnAsO_x@SiO_2$ drug delivery system. To quantify the drug loading efficiency of this system, we measured the amount of Mn and As loaded into HSNs by inductively coupled plasma mass spectroscopy (ICP-MS). ICP-MS analysis showed that the HSNs could load ATO prodrug with molar ratios of Mn/SiO_2 and As/SiO_2 as high as 1.45 ± 0.10 and 1.07 ± 0.06, respectively. It should be mentioned that the accurate Mn/As molar ratio is 1.35:1, suggesting that the $MnAsO_x$ present in the system is a mixture of two typical formations of manganese arsenite, $MnHAsO_3$ and $Mn_3(AsO_3)_2$.

Release Profiles. An acidic environment can trigger the collapse of $MnAsO_x$ complexes and the release of As and Mn ions from $MnAsO_x@SiO_2$. To quantitatively determine the release behavior of $MnAsO_x@SiO_2$, we measured ion release at pH 7.4 and 5.4, which represent the physiological environments of cell culture medium and the lysosome, respectively (Figure 1c). The release profiles showed negligible release of As and Mn ions (11% and 9.5% for As and Mn ions, respectively) from $MnAsO_x@SiO_2$ at physiological pH (pH 7.4), suggesting that ATO prodrug was stably entrapped in the HSNs in a neutral environment. The small release is likely due to the slight leakage at 37 °C. When the pH dropped to 5.4, the release process was remarkably accelerated and reached a plateau (78% and 82% for Mn and As ions, respectively) within 7 h. This pH-dependent release behavior demonstrates that $MnAsO_x@SiO_2$ can respond to an acidic environment, such as lysosome. Of particular importance, the released Mn ions can turn on the T_1 signal by increasing the efficiency of dipole−dipole interactions between Mn ions and the surrounding protons. Since the amount of released Mn ions is proportional to the amount of As ions, this characteristic permits $MnAsO_x@SiO_2$ to achieve real-time monitoring and quantitative assessment of drug release *in vitro*.

Activatable T_1 Imaging *in Vitro*. We incubated Mn ions and $MnAsO_x@SiO_2$ with buffer at pH 7.4 and 5.4 and

evaluated the relaxivity by a 0.5 T MRI scanner (Figure 1d and Supporting Information, Figure S3). Quantitative analysis indicated that there was no appreciable difference between the T_1 relaxivity (r_1) values for free Mn ions at pH 7.4 and 5.4 (11.5 and 11.1 mM^{-1} s^{1-} for pH 7.4 and 5.4, respectively). However, the r_1 value of $MnAsO_x$@SiO_2 in an acidic environment is significantly larger than that in a neutral environment (4.8 and 12.0 mM^{-1} s^{1-} for pH 7.4 and 5.4, respectively). According to the Solomon–Bloembergen–Morgan (SBM) theory, the longitudinal relaxation (R_1) efficiency is mainly dependent on the chemical exchange between metal centers and surrounding protons.[47,48] For this rationally designed MDDS, the water-insoluble $MnAsO_x$ in the HSNs could significantly inhibit the chemical exchange between Mn ions and protons, resulting in a much low r_1 value than that of free Mn ions at neutral pH. Once in an acidic environment, the $MnAsO_x$ collapses and releases free Mn ions, which could allow for efficient chemical exchange between the Mn ions and surrounding protons, thus lightening the T_1-weighted MR images (Scheme 1). This extraordinary capability enables this smart MDDS to qualitatively survey ATO release by activatable T_1 imaging.

We then tested the ability of the MDDS to monitor dynamic ATO release in a real-time manner. We incubated $MnAsO_x$@SiO_2 in citrate buffer (pH 5.4) for 0, 4, and 8 h, which corresponded to approximately 0, 55%, and 76% Mn release (or 0, 60%, and 80% As release), respectively. T_1-weighted MR images revealed a gradual enhancement of signal intensity with the r_1 values of 5.9, 10.1, and 12.2 mM^{-1} s^{1-} over time (Figure 1e,f). This gradual enhancement of T_1 signal can be ascribed to the increasing amount of free Mn ions progressively released from $MnAsO_x$@SiO_2. Since the amount of free Mn ions is proportional to the amount of released As ions, this MDDS can perform real-time monitoring of ATO release by examining T_1 signal enhancement under various conditions.

Subsequently, we monitored ATO release inside living cells. We first incubated SMMC-7721 cells with $MnAsO_x$@SiO_2 at different times and then collected the treated cells in small tubes and conducted the MR phantom imaging. The T_1 signal in T_1-weighted MR images was negligible during the first 2 h but then gradually brightened with the elapse of time (Figure 1g). These time-dependent signal changes reflected the slow release of Mn ions and ATO in cells. We also measured the total amount of Mn ions in the cells before and after treatment by ICP-MS. It appears that the PBS-treated cells contained 280.2 ± 5.3 ng of Mn ions, likely due to Mn being a natural cellular constituent and acting as a cofactor for enzymes and receptors.[50,51] Remarkably, the amount of Mn ions in cells dramatically increased to 701.3 ± 4.8, 937.9 ± 5.8, 1112.9 ± 8.3, and 931.1 ± 9.5 ng at 2, 4, 6, and 8 h after incubation with $MnAsO_x$@SiO_2, respectively (Figure 1h). This result is inconsistent with the changes in T_1 signal, especially at 4 and 8 h. Compared to the cells incubated with $MnAsO_x$@SiO_2 for 8 h, the treated cells for 4 h contained slightly more Mn ions but exhibited a significantly lower T_1 signal. These seemingly contradictory results could be attributed to the fact that ICP-MS detects the total amount of Mn ions, while activatable T_1 imaging reports only the amount of released Mn ions. These results strongly suggest that signal enhancement is generated by released and free Mn ions, rather than $MnAsO_x$@SiO_2. It is worth noting that the decreased amount of Mn ions at 8 h could be attributed to As ion toxicity in cancer cells,[46] which increases cell membrane permeability and allows Mn ions to escape from cells.

***In Vitro* Cytotoxicity.** Prior to test the cytotoxicity of MnAsOx@SiO_2, we investigated the cytotoxicity of HSNs and Mn ions by the 3-(4,5-dimethylthiazol-2-yl)-2,5-diphenyltetrazolium bromide (MTT) assay. HSNs and Mn ions showed negligible cytotoxicity after 48 h of incubation, even at concentrations up to 200 μg SiO_2/mL and 228 μM of Mn, respectively, suggesting that the drug carrier has acceptable biocompatibility and minimal side effects (Supporting Information, Figure S4). To evaluate the cytotoxicity of $MnAsO_x$@SiO_2, we exposed HeLa, HepG2, SMMC-7721, and H22 cells to $MnAsO_x$@SiO_2 or free ATO for 48 h and subsequently performed the MTT assay. $MnAsO_x$@SiO_2 exhibited stronger cytotoxic effects than free ATO for all four cell types, which is likely due to high cellular uptake of $MnAsO_x$@SiO_2 and slow ATO drug release (Figure 2).

To quantify cytotoxicity, we calculated the half-maximal inhibitory concentration (IC_{50}) values of $MnAsO_x$@SiO_2 and free ATO in HeLa, HepG2, SMMC-7721, and H22 cells (Supporting Information, Table S1). In all four cell lines, the IC_{50} values (48 h) of $MnAsO_x$@SiO_2 (0.9 ± 0.1, 20.0 ± 2.3, 2.5 ± 0.2, and 2.9 ± 0.3 μM, respectively) were significantly lower than those of free ATO (2.5 ± 0.3, 75.0 ± 6.8, 22.0 ± 1.5, and 7.7 ± 0.5 μM, respectively). $MnAsO_x$@SiO_2 cytotoxicity was found to be as high as 3.8 times that of the free drug. These results indicate that this rationally designed MDDS can kill cancer cells effectively *in vitro* and is therefore a potential candidate for tumor treatment in living subjects. We noted that these four cell lines have different IC_{50} values compared to the drug, which could be attributed to the diverse drug susceptibilities of different cell lines.

Surface Modification to Improve Behavior *in Vivo*. Surface modification of nanomaterials can reduce protein absorption and increase their circulation time *in vivo*. These modifications can improve anticancer drug delivery to tumors by an enhanced permeability and retention (EPR) effect.[52–54] We used a well-known biological reagent, glutathione (GSH), to functionalize the surface of $MnAsO_x$@SiO_2 (denoted

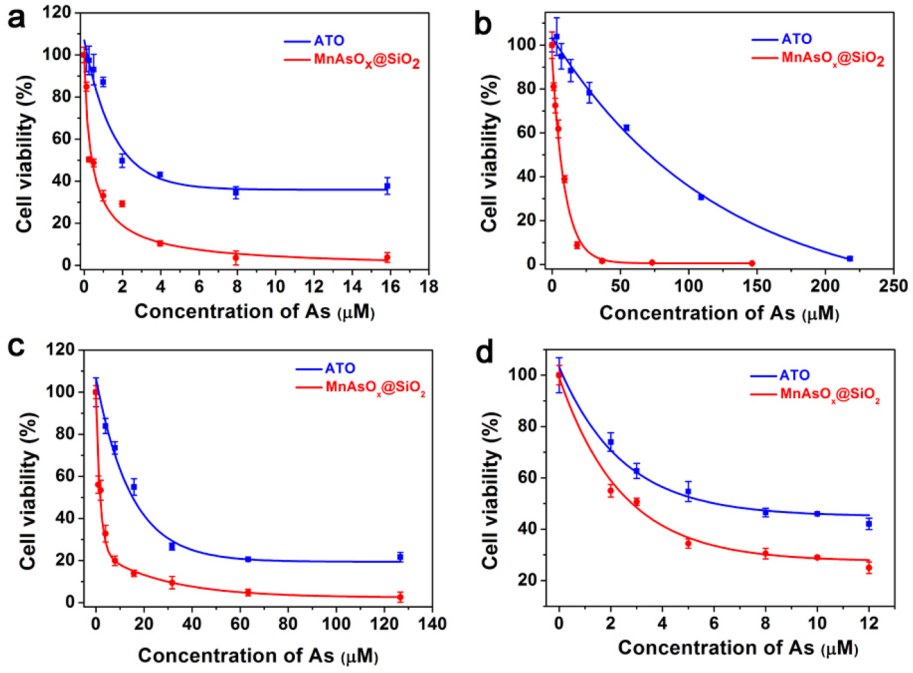

Figure 2. *In vitro* cytotoxicity assay. (a) HeLa, (b) HepG2, (c) SMMC-7721, and (d) H22 cells treated with free ATO and $MnAsO_x@SiO_2$ for 48 h (n = 5/group).

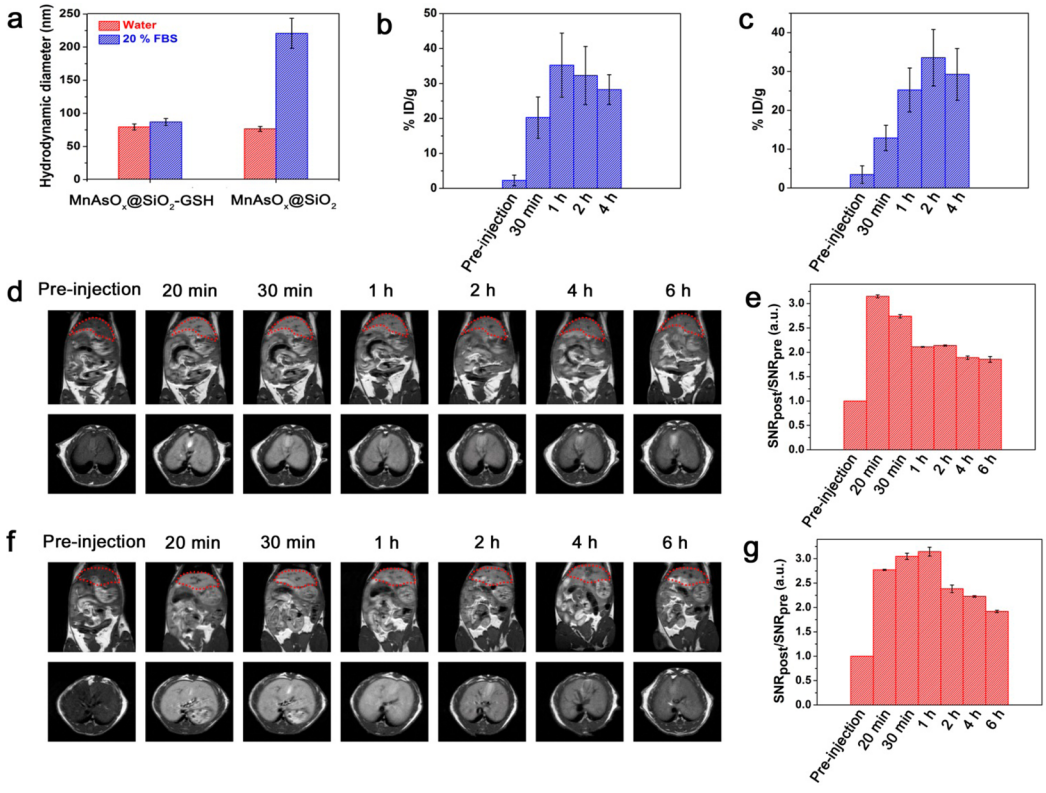

Figure 3. Monitoring drug release in liver of normal mice. (a) The DLS distribution of $MnAsO_x@SiO_2$ and $MnAsO_x@SiO_2$−GSH incubated with or without FBS, indicating that the GSH modification can reduce the interaction between $MnAsO_x@SiO_2$−GSH and serum proteins. The ICP-MS analysis of liver uptake of As element after accumulation of (b) $MnAsO_x@SiO_2$ and (c) $MnAsO_x@SiO_2$−GSH in liver (n = 3/group). *In vivo* T_1-weighted MR images of BALB/c mice at different times after intravenous injection of (d) $MnAsO_x@SiO_2$ and (f) $MnAsO_x@SiO_2$−GSH in coronal and transverse planes. Quantification of relative SNR_{liver} collected at different times after administration of (e) $MnAsO_x@SiO_2$ and (g) $MnAsO_x@SiO_2$−GSH in BALB/c mice (n = 3/group).

MnAsOx@SiO$_2$−GSH). $MnAsO_x@SiO_2$−GSH showed excellent colloidal stability in aqueous solution. We did not observe any aggregation or structural changes after storage for more than one month. More importantly,

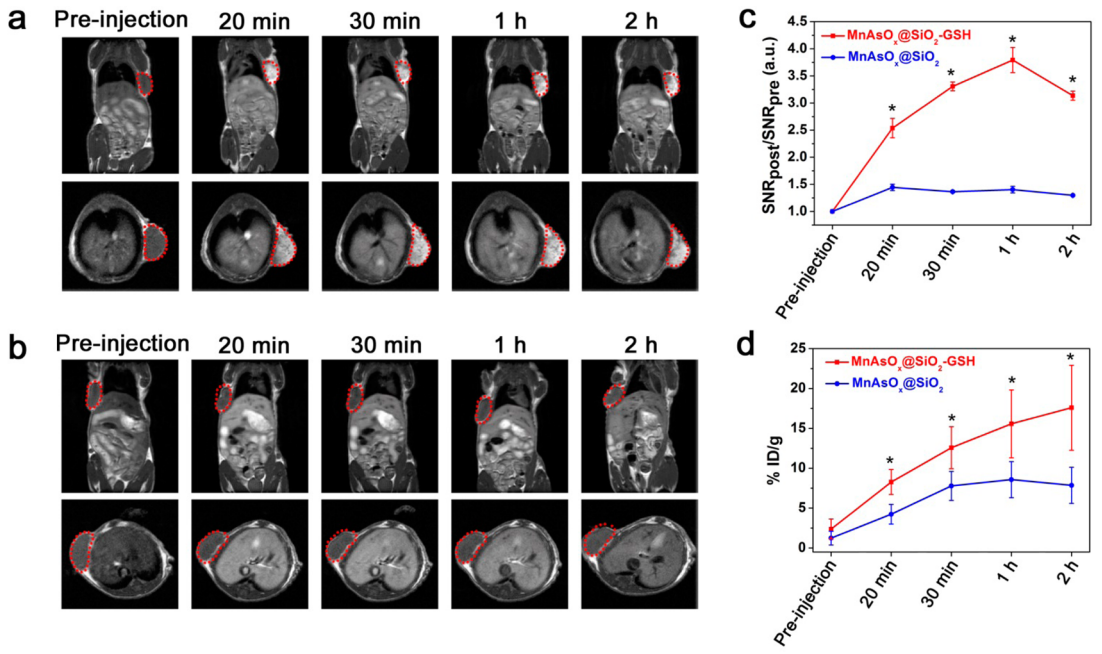

Figure 4. Diagnosis of tumor and monitoring drug release in mice with subcutaneous tumors. T_1-weighted MR images of BALB/c mice bearing H22 tumors at different times after intravenous injection of (a) $MnAsO_x@SiO_2$–GSH and (b) $MnAsO_x@SiO_2$ in coronal and transverse planes. (c) Quantification of relative SNR_{tumor} collected at different times after administration of $MnAsO_x@SiO_2$ and $MnAsO_x@SiO_2$–GSH in tumor (*$p < 0.05$, $n = 3$/group). (d) ICP-MS analysis of tumor uptake of As after injection of $MnAsO_x@SiO_2$ and $MnAsO_x@SiO_2$–GSH (*$p < 0.05$, $n = 3$/group).

there was no appreciable difference in HD between $MnAsO_x@SiO_2$–GSH incubated with or without fetal bovine serum (FBS) at 37 °C for 4 h. In comparison with $MnAsO_x@SiO_2$–GSH, $MnAsO_x@SiO_2$ exhibited a significant increase in HD after incubation with FBS (Figure 3a and Supporting Information, Figure S5). These results indicated that GSH reduced the nonspecific interaction between $MnAsO_x@SiO_2$–GSH and serum proteins, which was beneficial to prolong circulation time of the material and improve its EPR effect. We further investigated the half-life of $MnAsO_x@SiO_2$ and $MnAsO_x@SiO_2$–GSH in blood by detecting the concentrations of Mn and As ions. As expected, the blood circulation half-life of $MnAsO_x@SiO_2$–GSH was approximately 1.5 h, which is almost three times as long as that of $MnAsO_x@SiO_2$ (0.5 h). These results suggested that $MnAsO_x@SiO_2$–GSH was more suitable for cancer diagnosis and treatment compared to $MnAsO_x@SiO_2$ through an EPR effect (Supporting Information, Figure S6). Since free ions exhibit a short half-life of about several minutes in blood circulation,[55] these results indicated that Mn and As ions were stably entrapped in HSNs during circulation.

Drug Release *in Vivo*. We injected $MnAsO_x@SiO_2$ and $MnAsO_x@SiO_2$–GSH into BALB/c mice intravenously at a dose of 1.0 mg Mn/kg body weight (corresponding to 1.0 mg As/kg). Because of the high enrichment of nanomaterials in the liver,[56] we focused on the liver as the targeted region. ICP-MS analysis indicated that both samples resulted in significant accumulation of As ions in the liver after injection (Figure 3b,c). We then conducted T_1-weighted MRI at different time points and monitored the drug release process in real time. Both coronal and transverse images showed that the liver region exhibited a noticeably brighter signal after the injection of $MnAsO_x@SiO_2$ or $MnAsO_x@SiO_2$–GSH (Figure 3d,f). Moreover, the images showed a gradual enhancement of T_1 signal with increasing incubation time. These results clearly demonstrated that Mn ions and ATO were slowly released from the nanomaterials in the liver. To quantify the contrast enhancement, we calculated the signal-to-noise ratio (SNR) by analyzing the area of the images corresponding to the liver (Supporting Information, Table S2). The measured SNR values of the $MnAsO_x@SiO_2$ group were 314.6 ± 2.9%, 273.8 ± 3.4%, 211.0 ± 0.7%, 213.8 ± 1.2%, 188.9 ± 3.5%, and 185.4 ± 6.0% at 20 min, 30 min, 1, 2, 4, and 6 h post injection (p.i.), respectively (Figure 3e). In comparison with the $MnAsO_x@SiO_2$ group, the $MnAsO_x@SiO_2$–GSH group showed significantly different drug release kinetics, with SNR values of 277.1 ± 1.0%, 304.8 ± 6.5%, 314.5 ± 9.0%, 238.3 ± 7.8%, 222.5 ± 1.6%, and 191.9 ± 2.3%, at 20 min, 30 min, 1, 2, 4, and 6 h p.i., respectively (Figure 3g). These differences in drug release kinetics could be a result of the different behaviors of the materials when circulating through the blood. $MnAsO_x@SiO_2$–GSH exhibited a longer circulation time than $MnAsO_x@SiO_2$, which could slow down the uptake rate of $MnAsO_x@SiO_2$–GSH by the liver and extend the duration of drug release. As T_1 signal enhancement is proportional to the amount of

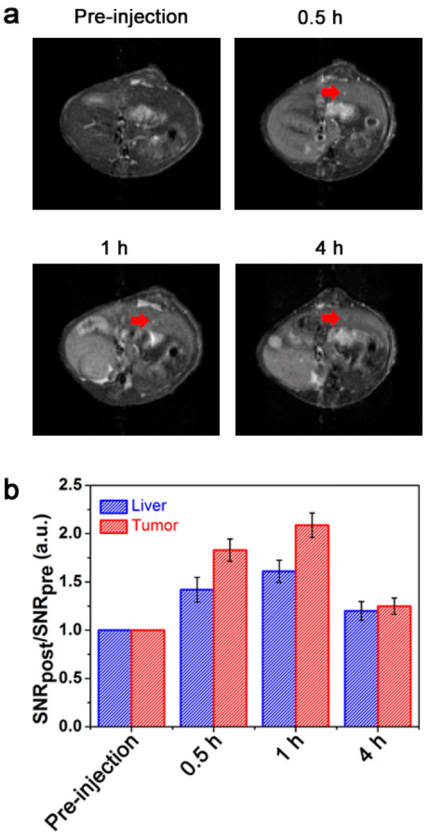

Figure 5. Diagnosis of tumor and monitoring drug release in mice with orthotopic tumors. (a) T_1-weighted MR images of BALC/c mice bearing H22 orthotopic tumors at different times after intravenous injection of $MnAsO_x@SiO_2$−GSH in transverse plane. The red arrows indicated the orthotopic liver tumor. (b) Quantification of relative SNR_{liver} and SNR_{tumor} collected at different times before and after injection of $MnAsO_x@SiO_2$−GSH (n = 3/group).

Mn and As ions released, the time-dependent enhancement of the T_1 signal allowed for real-time monitoring of the drug release process. It should be mentioned that the injection dose (1 mg Mn/kg each) in this study is estimated to be equivalent to a human dose of 0.08 mg/kg, which is much lower than the clinical dose of 0.275 mg/kg for Mn-DPDP (a commercial Mn based T_1 contrast agent).[57] We noted that the SNR values decreased after 1 h p.i. This phenomenon was probably caused by the metabolism of Mn^{2+} ions, indicating that the optimal imaging window is within 2 h after administration.

Tumor Imaging and Drug Release Monitoring in Tumors. Based on the above results, $MnAsO_x@SiO_2$ and $MnAsO_x@SiO_2$−GSH successfully and reproducibly generated MR contrast and enabled *in vivo* drug monitoring. Thus, these materials have great potential for accurate tumor diagnosis and dynamic drug release monitoring in tumors. We injected $MnAsO_x@SiO_2$ and $MnAsO_x@SiO_2$−GSH intravenously into BALB/c mice bearing murine hepatocellular carcinoma tumors, H22 tumors, at a dose of 1.0 mg Mn/kg body weight and conducted T_1-weighted MRI. The injection dose is estimated to be equivalent to a human dose of 0.08 mg/kg of both Mn and As ions, which is significantly lower than their clinical doses (0.27 mg/kg for Mn ions and 0.15 mg/kg for As ions).[57] Compared to the $MnAsO_x@SiO_2$ group, the $MnAsO_x@SiO_2$−GSH group showed lower T_1 signal enhancement in the liver, indicating that $MnAsO_x@SiO_2$−GSH delivered less ATO to the liver than $MnAsO_x@SiO_2$ (Figure 4a,b and Supporting Information, Figure S7). T_1-weighted MR images of the tumor region showed that the MR signal slowly increased over time and exhibited remarkable T_1 contrast from the surrounding normal tissue, especially the mice treated by $MnAsO_x@SiO_2$−GSH (Figure 4a,b). These results indicated that ATO was successfully delivered to the tumor and that drug release in the tumor could be visualized in real time. Since the efficacy of chemotherapeutics is highly dependent on the efficiency of drug release in the tumor, these images are necessary for evaluating the therapeutic efficiency of the drug. To quantify the contrast enhancement, we calculated SNR by analyzing the region of the images corresponding to the tumor. The SNR values from the $MnAsO_x@SiO_2$−GSH group were 253.8 ± 17.8%, 330.6 ± 8.1%, 379.4 ± 23.2%, and 313.5 ± 8.4% at 20, 30, 60, and 120 min p.i., respectively, which were much higher than those from the $MnAsO_x@SiO_2$ group (124.4 ± 2.9%, 116.4 ± 1.6%, 120.3 ± 6.1%, and 119.7 ± 0.7% at 20, 30, 60, and 120 min p.i., respectively). The extremely high T_1 signal enhancement in the $MnAsO_x@SiO_2$−GSH group demonstrates that $MnAsO_x@SiO_2$−GSH is an excellent tool for accurate tumor diagnosis and monitoring of drug release (Figure 4c and Supporting Information, Table S3). We then measured the amount of As ions in the tumor and evaluated the relationship between the T_1 signal and the amount of ATO. In comparison with the preinjected state, the mice treated with $MnAsO_x@SiO_2$−GSH had much higher amounts of As in the tumor than those treated with $MnAsO_x@SiO_2$ (Figure 4d). This result is in good agreement with our finding that T_1 signal enhancement in the tumor was much higher in the $MnAsO_x@SiO_2$−GSH group compared to the $MnAsO_x@SiO_2$ group. Overall, these results demonstrate that this carefully designed MDDS is able to report different amounts of drug by monitoring the changes in T_1 signal. We observed slight differences between the As uptake curve and the T_1 signal enhancement in the treated mice. This phenomenon could be due to the fact that ICP-MS detects the total amount of As ions while activatable T_1 imaging reports only the amount of released As ions. Since only the released As ions can effectively kill cancer cells, this real-time monitoring approach is much more suitable and accurate than ICP-MS for monitoring *in vivo* drug bioavailability.

We conducted an additional study examining T_1-weighted MRI and drug release in an orthotopic

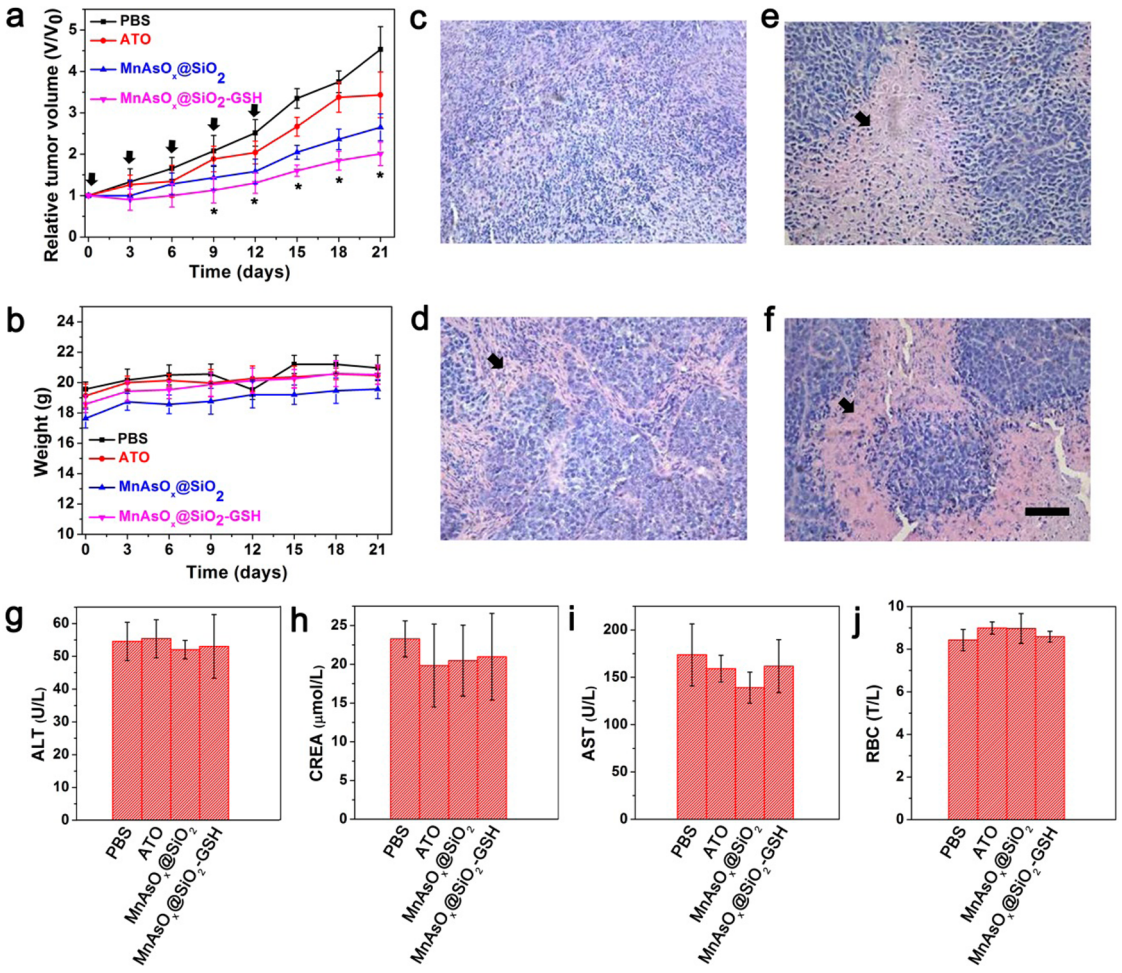

Figure 6. ***In vivo*** **therapeutic study. (a) Tumor growth curves after intravenous injection of PBS, ATO, $MnAsO_x@SiO_2$, or $MnAsO_x@SiO_2$−GSH with a dose of 2.0 mg As per kg for 21 days. Arrows indicate the day for treatment (*$p < 0.05$, $n = 6$/group). (b) Body weight change curves of the mice during treatment by PBS, ATO, $MnAsO_x@SiO_2$, or $MnAsO_x@SiO_2$−GSH. Tumor H&E histology images of the mice after administration of (c) PBS, (d) ATO, (e) $MnAsO_x@SiO_2$, and (f) $MnAsO_x@SiO_2$−GSH for 21 days. Black arrows indicate the typical necrotic cells in tumors. Scale bar, 200 μm. Quantitative analysis of biochemistry indices (g) aspartate transaminase, (h) alanine aminotransferase, (i) creatinine, and (j) red blood cells of the mice treated by PBS, ATO, $MnAsO_x@SiO_2$, and $MnAsO_x@SiO_2$−GSH for 21 days.**

H22 tumor model. We established the orthotopic liver tumor model by injection of H22 cells (1×10^6) into the liver of BALB/c mice. When the hepatic tumor reached 1−2 mm in diameter, we injected $MnAsO_x@SiO_2$−GSH intravenously into the mice (1.0 mg Mn per kg) and scanned the animals with a 7 T microMRI scanner (Supporting Information, Figure S8). The T_1-weighted MR signal was bright in both the tumor and liver after administration. Remarkably, signal enhancement in the tumor was much higher than that in the liver, leading to easy differentiation between liver lesions and normal liver tissue (Figure 5a). This unique phenomenon occurs because the extracellular environment of the tumor is more acidic (pH 6.5−6.8) than normal tissue (pH ∼ 7.4),[3,58] which results in faster release of Mn ion (As ions) and larger T_1 signal enhancement. It should be noted of that the T_1 MR signal of the tumor gradually increased until 1 h p.i., reflecting ATO release and demonstrating that this MDDS can also allow real-time monitoring of drug release in orthotopic hepatic tumors (Figure 5b and Supporting Information, Table S4). We noted that signal enhancement in the tumor dropped after 1 h p.i. It is necessary to conduct MRI scanning within 1 h to diagnose hepatic tumor, which meets the basic requirements of clinical diagnosis.

In Vivo **Therapy.** We then performed an *in vivo* study evaluating the therapeutic effect of this system in nude mice bearing human hepatocellular carcinoma tumors, SMMC-7721 tumors. We injected PBS, ATO, $MnCl_2$, HSNs, $MnAsO_x@SiO_2$, or $MnAsO_x@SiO_2$−GSH intravenously into the mice (2.0 mg As/kg each) at days 0, 3, 6, 9, and 12 (Figure 6 and Supporting Information, Figure S9). All three drugs inhibited SMMC-7721 tumor growth (Figure 6a). On the contrary, the tumors in mice treated with PBS, free Mn ions, and HSNs grew rapidly (Supporting Information, Figure S10a). Despite $MnAsO_x@SiO_2$−GSH and $MnAsO_x@SiO_2$ having similar cytotoxic effects on cancer cells, the former was

more effective in delaying tumor growth (Supporting Information, Figure S11). This result could be attributed to the fact that the GSH-modified HSN nanocarriers exhibited prolonged circulation time and increased drug accumulation at the tumor site by the EPR effect. Importantly, the treated mice maintained a consistent weight over the course of the treatment, indicating that the MDDS had minimal side effects (Figure 6b and Supporting Information, Figure S10b). To further assess systemic toxicity in the animals, we conducted hematoxylin and eosin (H&E) staining and main biochemistry index analysis after treatment. All major organs maintained their typical structural phenotypes and did not exhibit appreciable microscopic lesions, while the tumor tissues showed a typical necrotic response after treatment with ATO, $MnAsO_x@SiO_2$, or $MnAsO_x@SiO_2$–GSH (Figure 6c–f and Supporting Information, Figure S12). In agreement with the histological analysis, the main biochemistry indices, including aspartate transaminase (ALT), alanine aminotransferase (AST), creatinine (CREA), and red blood cells (RBC), were maintained at similar levels as the controls, suggesting that the treatments did not affect liver and kidney functions (Figure 6g–j and Supporting Information, Figure S13). These results indicate that this MDDS exhibits minimal side effects and acceptable biocompatibility.

CONCLUSIONS

In summary, we reported a novel strategy to monitor the *in vitro* and *in vivo* release of the anticancer drug ATO in a real-time manner by activatable T_1 imaging. Due to its unique features, including compatibly inorganic property, controllable drug release behavior, and proper surface functionalization, this MDDS significantly increased the anticancer activity of ATO *in vitro* and *in vivo*. Of particular significance, this rationally designed MDDS can simultaneously release Mn ions in an acidic tumor microenvironment, which effectively turns on the T_1 MR signal and facilitates activatable T_1 imaging. This unique feature makes it possible for accurate tumor imaging and diagnosis. More importantly, the T_1 signal enhancement is correlated to the amount of released drug, which allows the smart MDDS to monitor the drug release process in real time, which is a current major challenge in drug delivery. This new drug delivery system incorporating cancer diagnosis, real-time drug release monitoring, and efficient anticancer ability in one smart entity can open up new venues in cancer treatment and management.

EXPERIMENTAL METHODS

Reagent. Oleic acid (tech 90%), tetraethyl orthosilicate (TEOS 99.9%), (3-aminopropyl)triethoxysilane (APTES 97%), manganese(II) chloride tetrahydrate (tech 90%), As_2O_3 (tech 90%), and 3-maleimidobutyric acid *N*-succinimidyl ester were purchased from Alfa Aesar. Polyoxyethylene(5)nonylphenyl ether (Co-520) was purchased from Sigma-Aldrich. Ammonium hydroxide and and ethanol were purchased from Sinopharm Chemical Reagent Co. Ltd. (Shanghai, China). All chemicals were used as received without further purification.

Characterizations. TEM images were captured on a JEM-2100 microscope at an accelerating voltage of 200 kV. The element mapping analysis was performed on a Tecnai F20 microscope at an accelerating voltage of 300 kV. The element analysis of Mn and As was determined by ICP-MS. The DLS measurements were performed on a Malvern Zetasizer nano ZS instrument. The MRI testing and T_1 relaxation time measurements were tested at a 0.5 T NMR120-Analyst NMR Analyzing and Imaging system (Niumag Corporation, Shanghai, China). *In vivo* MR images measurements were performed on a 7T MRI scanner (Varian 7T micro MRI System).

Synthesis of Hollow SiO_2–NH_2 Nanoparticles (HSNs). Uniform HSNs were prepared *via* selective etching of as-synthesized $Fe_3O_4@SiO_2$–NH_2 template with 10% HCl. We mixed 5 mg of $Fe_3O_4@SiO_2$–NH_2 with 6 mL of concentrated hydrochloric acid for 4 h. The nanomaterials were separated by centrifugation and washed three times with ethanol. After washing, this nanomaterial was dissolved in ultrapure water for long-term storage at room temperature.

Preparation of $MnAsO_x@SiO_2$ Multifunctional Drug Delivery System (MDDS). The $MnAsO_x@SiO_2$ MDDS was prepared *via* the ion gradient-mediated loading methodology using the as-synthesized hollow silica nanoparticles. We hydrated the HSNs in 300 mM aqueous manganese chloride tetrahydrate solution (pH ~ 7.4) by ultrasound. After the mixture was subjected to 10 freeze–thaw cycles, we centrifuged (14000 rpm, 20 min) the reaction solution to remove the excess manganese chloride and dissolved the sample in ultrapure water. Then, we added aqueous arsenic trioxide (ATO, pH ~ 8) and incubated it at 50 °C for 6 h. After the insoluble manganese arsenite complex was discarded, we collected the $MnAsO_x@SiO_2$ by centrifugation. The $MnAsO_x@SiO_2$ MDDS was kept in ultrapure water at 4 °C for further use.

Preparation of $MnAsO_x@SiO_2$–GSH MDDS. The $MnAsO_x@SiO_2$–GSH was prepared by modifying the as-synthesized $MnAsO_x@SiO_2$ through the functional amino groups. We mixed the $MnAsO_x@SiO_2$ (1 nmol) and the heterobifunctional linker, 3-maleimidobutyric acid *N*-succinimidyl ester (1 μmol), in borate buffer (pH ~ 7.5) and incubated the mixture at room temperature for 2 h with gentle shaking. After purification, we added glutathione (GSH) molecules (0.1 μmol) into the solution containing activated nanoparticles and maintained general shaking for 2 h at room temperature. After the excess GSH was removed by centrifugation, we stored the $MnAsO_x@SiO_2$–GSH in PBS buffer for *in vitro* and *in vivo* biological evaluation.

***In Vivo* Liver MR Imaging.** Animal experiments were executed according to the protocol approved by the Institutional Animal Care and Use Committee of Xiamen University. BALB/c mice (6 weeks old, 18–22 g) were purchased from Laboratory Animal Center of Xiamen University. We performed the *in vivo* MR imaging of liver by using BALB/c mouse as a model. We intravenously injected $MnAsO_x@SiO_2$ and $MnAsO_x@SiO_2$–GSH at a dose of 1 mg Mn/kg body weight. The coronal and transverse plane MR images were scanned using a sequence (TR/TE = 400/10 ms, 256 × 256 matrices, averages = 1, FOV = 60 × 60) on a Varian 7 T microMRI scanner. The MR images were obtained at preinjection, 20 min, 30 min, 1, 2, 4, and 6 h postinjection (n = 3/group). To quantify the signal enhancement, we calculated the signal-to-noise ratio (SNR) by the equation $SNR_{liver} = SI_{liver}/SD_{noise}$, where SI represents signal intensity and SD represents standard deviation.

***In Vivo* Therapeutic Study.** Female nude mice (6 weeks old, 18–22 g) were purchased from the Laboratory Animal Center of

Xiamen University. We established the tumor model by injecting human hepatocellular carcinoma cells, SMMC-7721 cells (5×10^6), in the subcutaneous tissue. When the SMMC-7721 carcinoma reached approximately 0.5 cm in diameter, we intravenously injected PBS, ATO, HSNs, $MnCl_2$, $MnAsO_x@SiO_2$, or $MnAsO_x@SiO_2$−GSH into the mice (2 mg As/kg body weight each) and monitored mouse weight and tumor size (n = 6/group). The tumor volumes were calculated by the equation of $V_{Tumor} = (a^2 \times b)/2$ (a and b represents the maximum and minimum diameter of the tumor, respectively).

Conflict of Interest: The authors declare no competing financial interest.

Supporting Information Available: Experimental details, EDS analysis, DLS measurements, MRI relaxivity, MR image of tumor, *in vivo* therapy, H&E staining, and biochemistry indices analysis. This material is available free of charge *via* the Internet at http://pubs.acs.org.

Acknowledgment. This work was supported by the National Key Basic Research Program of China (2013CB933900 and 2014CB744502), National Natural Science Foundation of China (21222106, 81370042, 81430041, 81472231, and 81201805), Natural Science Foundation of Fujian (2013J06005 and 2013D014), Fok Ying Tung Education Foundation (142012), and National Key Sci-Tech Special Project of China (2012ZX10002-011-005).

REFERENCES AND NOTES

1. Hubbell, J. A.; Langer, R. Translating Materials Design to the Clinic. *Nat. Mater.* **2013**, *12*, 963–966.
2. Irvine, D. J. Drug Delivery: One Nanoparticle, One Kill. *Nat. Mater.* **2011**, *10*, 342–343.
3. Mura, S.; Nicolas, J.; Couvreur, P. Stimuli-Responsive Nanocarriers for Drug Delivery. *Nat. Mater.* **2013**, *12*, 991–1003.
4. Zhao, Z.; Huang, D.; Yin, Z.; Chi, X.; Wang, X.; Gao, J. Magnetite Nanoparticles as Smart Carriers to Manipulate the Cytotoxicity of Anticancer Drugs: Magnetic Control and pH-Responsive Release. *J. Mater. Chem.* **2012**, *22*, 15717–15725.
5. Wang, F.; Wang, Y.; Dou, S.; Xiong, M.; Sun, T.; Wang, J. Doxorubicin-Tethered Responsive Gold Nanoparticles Facilitate Intracellular Drug Delivery for Overcoming Multidrug Resistance in Cancer Cells. *ACS Nano* **2011**, *5*, 3679–3692.
6. Zrazhevskiy, P.; Sena, M.; Gao, X. Designing Multifunctional Quantum Dots for Bioimaging, Detection, and Drug Delivery. *Chem. Soc. Rev.* **2010**, *39*, 4326–4354.
7. Zhang, P.; Cheng, F.; Zhou, R.; Cao, J.; Li, J.; Burda, C.; Min, Q.; Zhu, J. DNA-Hybrid-Gated Multifunctional Mesoporous Silica Nanocarriers for Dual-Targeted and MicroRNA-Responsive Controlled Drug Delivery. *Angew. Chem., Int. Ed.* **2014**, *53*, 2371–2375.
8. Gao, J.; Liang, G.; Cheung, J. S.; Pan, Y.; Kuang, Y.; Zhao, F.; Zhang, B.; Zhang, X.; Wu, E. X.; Xu, B. Multifunctional Yolk−Shell Nanoparticles: A Potential MRI Contrast and Anticancer Agent. *J. Am. Chem. Soc.* **2008**, *130*, 11828–11833.
9. Yang, P.; Gai, S.; Lin, J. Functionalized Mesoporous Silica Materials for Controlled Drug Delivery. *Chem. Soc. Rev.* **2012**, *41*, 3679–3698.
10. Wang, Z. Y.; Chen, Z. Acute Promyelocytic Leukemia: From Highly Fatal to Highly Curable. *Blood* **2008**, *111*, 2505–2515.
11. Miller, W. H.; Schipper, H. M.; Lee, J. S.; Singer, J.; Waxman, S. Mechanisms of Action of Arsenic Trioxide. *Cancer Res.* **2002**, *62*, 3893–3903.
12. Lu, J.; Chew, E. H.; Holmgren, A. Targeting Thioredoxin Reductase is a Basis for Cancer Therapy by Arsenic Trioxide. *Proc. Natl. Acad. Sci. U.S.A.* **2007**, *104*, 12288–12293.
13. Lee, S. M.; Lee, O. S.; O'Halloran, T. V.; Schatz, G. C.; Nguyen, S. T. Triggered Release of Pharmacophores from [Ni($HAsO_3$)]-Loaded Polymer-Caged Nanobin Enhances Pro-Apoptotic Activity: A Combined Experimental and Theoretical Study. *ACS Nano* **2011**, *5*, 3961–3969.
14. Zhao, Z.; Zhang, H.; Chi, X.; Li, H.; Yin, Z.; Huang, D.; Wang, X.; Gao, J. Silica Nanovehicles Endow Arsenic Trioxide with an Ability to Effectively Treat Cancer Cells and Solid Tumors. *J. Mater. Chem. B* **2014**, *2*, 6313–6323.
15. Riehemann, K.; Schneider, S. W.; Luger, T. A.; Godin, B.; Ferrari, M.; Fuchs, H. Nanomedicine—Challenge and Perspectives. *Angew. Chem., Int. Ed.* **2009**, *48*, 872–897.
16. Liu, J.; Bu, J.; Bu, W.; Zhang, S.; Pan, L.; Fan, W.; Chen, F.; Zhou, L.; Peng, W.; Zhao, K.; et al. Real-Time *in vivo* Quantitative Monitoring of Drug Release by Dual-Mode Magnetic Resonance and Upconverted Luminescence Imaging. *Angew. Chem., Int. Ed.* **2014**, *53*, 4551–4555.
17. Jana, A.; Devi, K. S. P.; Maiti, T. K.; Singh, N. D. P. Perylene-3-ylmethanol: Fluorescent Organic Nanoparticles as a Single-Component Photoresponsive Nanocarrier with Real-Time Monitoring of Anticancer Drug Release. *J. Am. Chem. Soc.* **2012**, *134*, 7656–7659.
18. Lai, J.; Shah, B. P.; Garfunkel, E.; Lee, K. Versatile Fluorescence Resonance Energy Transfer-Based Mesoporous Silica Nanoparticles for Real-Time Monitoring of Drug Release. *ACS Nano* **2013**, *7*, 2741–2750.
19. Tang, J.; Kong, B.; Wu, H.; Xu, M.; Wang, Y.; Wang, Y.; Zhao, D.; Zheng, G. Carbon Nanodots Featuring Efficient FRET for Real-Time Monitoring of Drug Delivery and Two-Photon Imaging. *Adv. Mater.* **2013**, *25*, 6569–6574.
20. Bagalkot, V.; Zhang, L.; Levy-Nissenbaum, E.; Jon, S.; Kantoff, P. W.; Langer, R.; Farokhzad, O. C. Quantum Dot−Aptamer Conjugates for Synchronous Cancer Imaging, Therapy, and Sensing of Drug Delivery Based on Bi-Fluorescence Resonance Energy Transfer. *Nano Lett.* **2007**, *7*, 3065–3070.
21. Kim, J.; Kim, H. S.; Lee, N.; Kim, T.; Kim, H.; Yu, T.; Song, I. C.; Moon, W. K.; Hyeon, T. Multifunctional Uniform Nanoparticles Composed of a Magnetite Nanocrystal Core and a Mesoporous Silica Shell for Magnetic Resonance and Fluorescence Imaging and for Drug Delivery. *Angew. Chem., Int. Ed.* **2008**, *47*, 8438–8441.
22. Wang, C.; Xu, H.; Liang, C.; Liu, Y.; Li, Z.; Yang, G.; Cheng, L.; Li, Y.; Liu, Z. Iron Oxide@ Polypyrrole Nanoparticles as a Multifunctional Drug Carrier for Remotely Controlled Cancer Therapy with Synergistic Antitumor Effect. *ACS Nano* **2013**, *7*, 6782–6795.
23. Chang, Y.; Liu, N.; Chen, L.; Meng, X.; Liu, Y.; Li, Y.; Wang, J. Synthesis and Characterization of DOX-Conjugated Dendrimer-Modified Magnetic Iron Oxide Conjugates for Magnetic Resonance Imaging, Targeting, and Drug Delivery. *J. Mater. Chem.* **2012**, *22*, 9594–9601.
24. Lee, G. Y.; Qian, W. P.; Wang, L.; Wang, Y. A.; Staley, C. A.; Satpathy, M.; Nie, S.; Mao, H.; Yang, L. Theranostic Nanoparticles with Controlled Release of Gemcitabine for Targeted Therapy and MRI of Pancreatic Cancer. *ACS Nano* **2013**, *7*, 2078–2089.
25. Ling, D.; Park, W.; Park, S.; Lu, Y.; Kim, K. S.; Hackett, M. J.; Kim, B. H.; Yim, H.; Jeon, Y. S.; Na, K.; et al. Multifunctional Tumor pH-Sensitive Self-Assembled Nanoparticles for Bimodal Imaging and Treatment of Resistant Heterogeneous Tumors. *J. Am. Chem. Soc.* **2014**, *136*, 5647–5655.
26. Kim, D.; Jeong, Y. Y.; Jon, S. A Drug-Loaded Aptamer−Gold Nanoparticle Bioconjugate for Combined CT Imaging and Therapy of Prostate Cancer. *ACS Nano* **2010**, *4*, 3689–3696.
27. Kang, B.; Afifi, M. M.; Austin, L. A.; El-Sayed, M. A. Exploiting the Nanoparticle Plasmon Effect: Observing Drug Delivery Dynamics in Single Cells *via* Raman/Fluorescence Imaging Spectroscopy. *ACS Nano* **2013**, *7*, 7420–7427.
28. Probst, C. E.; Zrazhevskiy, P.; Bagalkot, V.; Gao, X. Quantum Dots as a Platform for Nanoparticle Drug Delivery Vehicle Design. *Adv. Drug Delivery Rev.* **2013**, *65*, 703–718.
29. Hu, S.; Kuo, K.; Tung, W.; Liu, D.; Chen, S. A Multifunctional Nanodevice Capable of Imaging, Magnetically Controlling, and *in situ* Monitoring Drug Release. *Adv. Funct. Mater.* **2009**, *19*, 3396–3403.
30. Dai, Y.; Ma, P. A.; Cheng, Z.; Kang, X.; Zhang, X.; Hou, Z.; Li, C.; Yang, D.; Zhai, X.; Lin, J. Up-Conversion Cell Imaging and

pH-Induced Thermally Controlled Drug Release from $NaYF_4$:Yb^{3+}/Er^{3+}@Hydrogel Core–Shell Hybrid Microspheres. *ACS Nano* **2012**, *6*, 3327–3338.
31. Louie, A. Y.; Huber, M. M.; Ahrens, E. T.; Rothbacher, U.; Moats, R.; Jacobs, R. E.; Fraser, S. E.; Meade, T. J. *In Vivo* Visualization of Gene Expression Using Magnetic Resonance Imaging. *Nat. Biotechnol.* **2000**, *18*, 321–325.
32. Razgulin, A.; Ma, N.; Rao, J. Strategies for *in vivo* Imaging of Enzyme Activity: An Overview and Recent Advances. *Chem. Soc. Rev.* **2011**, *40*, 4186–4216.
33. Rodríguez, E.; Nilges, M.; Weissleder, R.; Chen, J. W. Activatable Magnetic Resonance Imaging Agents for Myeloperoxidase Sensing: Mechanism of Activation, Stability, and Toxicity. *J. Am. Chem. Soc.* **2009**, *132*, 168–177.
34. Zhao, Z.; Fan, H.; Zhou, G.; Bai, H.; Liang, H.; Wang, R.; Zhang, X.; Tan, W. Activatable Fluorescence/MRI Bimodal Platform for Tumor Cell Imaging *via* MnO_2 Nanosheet–Aptamer Nanoprobe. *J. Am. Chem. Soc.* **2014**, *136*, 11220–11223.
35. Santra, S.; Jativa, S. D.; Kaittanis, C.; Normand, G.; Grimm, J.; Perez, J. M. Gadolinium-Encapsulating Iron Oxide Nanoprobe as Activatable NMR/MRI Contrast Agent. *ACS Nano* **2012**, *6*, 7281–7294.
36. Werner, E. J.; Datta, A.; Jocher, C. J.; Raymond, K. N. High-Relaxivity MRI Contrast Agents: Where Coordination Chemistry Meets Medical Imaging. *Angew. Chem., Int. Ed.* **2008**, *47*, 8568–8580.
37. Kim, K.; Fonda, J. R.; Lawler, E. V.; Gagnon, D.; Kaufman, J. S. Change in Use of Gadolinium-Enhanced Magnetic Resonance Studies in Kidney Disease Patients after US Food and Drug Administration Warnings: A Cross-Sectional Study of Veterans Affairs Health Care System Data From 2005–2008. *Am. J. Kidney Dis.* **2010**, *56*, 458–467.
38. Jalandhara, N.; Arora, R.; Batuman, V. Nephrogenic Systemic Fibrosis and Gadolinium-Containing Radiological Contrast Agents: An Update. *Clin. Pharmacol. Ther.* **2011**, *89*, 920–923.
39. Terreno, E.; Castelli, D. D.; Viale, A.; Aime, S. Challenges for Molecular Magnetic Resonance Imaging. *Chem. Rev.* **2010**, *110*, 3019–3042.
40. Skjold, A.; Amundsen, B. H.; Wiseth, R.; Støylen, A.; Haraldseth, O.; Larsson, H. B. W.; Jynge, P. Manganese Dipyridoxyl-Diphosphate (MnDPDP) as a Viability Marker in Patients with Myocardial Infarction. *J. Magn. Reson. Imaging* **2007**, *26*, 720–727.
41. Aoki, I.; Takahashi, Y.; Chuang, K.-H.; Silva, A. C.; Igarashi, T.; Tanaka, C.; Childs, R. W.; Koretsky, A. P. Cell Labeling for Magnetic Resonance Imaging with The T_1 Agent Manganese Chloride. *NMR Biomed.* **2006**, *19*, 50–59.
42. Bernardino, M. E.; Weinreb, J. C.; Mitchell, D. G.; Small, W. C.; Morris, M. Safety and Optimum Concentration of a Manganese Chloride–Based Oral MR Contrast Agent. *J. Magn. Reson. Imaging* **1994**, *4*, 872–876.
43. Loving, G. S.; Mukherjee, S.; Caravan, P. Redox-Activated Manganese-Based MR Contrast Agent. *J. Am. Chem. Soc.* **2013**, *135*, 4620–4623.
44. Kim, T.; Momin, E.; Choi, J.; Yuan, K.; Zaidi, H.; Kim, J.; Park, M.; Lee, N.; McMahon, M. T.; Quinones-Hinojosa, A.; et al. Mesoporous Silica-Coated Hollow Manganese Oxide Nanoparticles as Positive T_1 Contrast Agents for Labeling and MRI Tracking of Adipose-Derived Mesenchymal Stem Cells. *J. Am. Chem. Soc.* **2011**, *133*, 2955–2961.
45. Na, H. B.; Lee, J. H.; An, K.; Park, Y. I.; Park, M.; Lee, I. S.; Nam, D.; Kim, S. T.; Kim, S.; Kim, S.; et al. Development of a T_1 Contrast Agent for Magnetic Resonance Imaging Using MnO Nanoparticles. *Angew. Chem., Int. Ed.* **2007**, *46*, 5397–5401.
46. Chen, H.; MacDonald, R. C.; Li, S.; Krett, N. L.; Rosen, S. T.; O'Halloran, T. V. Lipid Encapsulation of Arsenic Trioxide Attenuates Cytotoxicity and Allows for Controlled Anticancer Drug Release. *J. Am. Chem. Soc.* **2006**, *128*, 13348–13349.
47. Solomon, I. Relaxation Processes in a System of Two Spins. *Phys. Rev.* **1955**, *99*, 559–565.
48. Bloembergen, N.; M, L. O. Proton Relaxation Times in Paramagnetic Solutions. Effects of Electron Spin Relaxation. *J. Chem. Phys.* **1961**, *34*, 842–850.
49. Koparde, V. N.; Cummings, P. T. Molecular Dynamics Study of Water Adsorption on TiO_2 Nanoparticles. *J. Phys. Chem. C* **2007**, *111*, 6920–6926.
50. Kanyo, Z. F.; Scolnick, L. R.; Ash, D. E.; Christianson, D. W. Structure of a Unique Binuclear Manganese Cluster in Arginase. *Nature* **1996**, *383*, 554–557.
51. Tari, L. W.; Matte, A.; Goldie, H.; Delbaere, L. T. J. Mg^{2+}-Mn^{2+} Clusters in Enzyme-Catalyzed Phosphoryl-Transfer Reactions. *Nat. Struct. Mol. Biol.* **1997**, *4*, 990–994.
52. Crayton, S. H.; Tsourkas, A. pH-Titratable Superparamagnetic Iron Oxide for Improved Nanoparticle Accumulation in Acidic Tumor Microenvironments. *ACS Nano* **2011**, *5*, 9592–9601.
53. Zhou, C.; Hao, G.; Thomas, P.; Liu, J.; Yu, M.; Sun, S.; Öz, O. K.; Sun, X.; Zheng, J. Near-Infrared Emitting Radioactive Gold Nanoparticles with Molecular Pharmacokinetics. *Angew. Chem., Int. Ed.* **2012**, *51*, 10118–10122.
54. Yu, M.; Zhou, C.; Liu, J.; Hankins, J. D.; Zheng, J. Luminescent Gold Nanoparticles with pH-Dependent Membrane Adsorption. *J. Am. Chem. Soc.* **2011**, *133*, 11014–11017.
55. Feng, Y. Z. Y.; Ke, T.; Jeong, E. K.; Parker, D. L.; Lu, Z. R. Pharmacokinetics, Biodistribution and Contrast Enhanced MR Blood Pool Imaging of Gd-DTPA Cystine Copolymers and Gd-DTPA Cystine Diethyl Ester Copolymers in a Rat Model. *Pharm. Res.* **2006**, *23*, 1736–1742.
56. Walkey, C. D.; Chan, W. C. W. Understanding and Controlling The Interaction of Nanomaterials with Proteins in a Physiological Environment. *Chem. Soc. Rev.* **2012**, *41*, 2780–2799.
57. Freireich, E. J.; Gehan, E. A.; Rall, D. P.; Schmidt, L. H.; Skipper, H. E. Quantitative Comparison of Toxicity of Anticancer Agents in Mouse, Rat, Hamster, Dog, Monkey, and Man. *Cancer Chemother. Rep.* **1966**, *50*, 219–244.
58. Gerweck, L. E.; Seetharaman, K. Cellular pH Gradient in Tumor *Versus* Normal Tissue: Potential Exploitation for the Treatment of Cancer. *Cancer Res.* **1996**, *56*, 1194–1198.